ADVANCED OPTICAL MATERIALS

COMMUNICATION

A New Route for Fabricating On-Chip Chalcogenide Microcavity Resonator Arrays

Ozan Aktas, Erol Ozgur, Osama Tobail, Mehmet Kanik, Ersin Huseyinoglu, and Mehmet Bayindir*

The development of strategies for mass production and multiple integration of optical microresonators in photonic circuits has been a subject of intense research, aiming to reach the full potential of their technological exploitation. Among the different types of optical microresonators,[1] especially surface-tension-induced whispering gallery mode (WGM) microresonators in the form of spheres[2] and toroids,[3] are the focus of interest, regarding their compact shapes with atomically smooth surfaces which enable the highest temporal and spatial confinement of light in terms of quality factor ($Q \leq 10^9$) and mode volume, reducing the threshold for nonlinear optical interactions such as third harmonic generation,[4] four wave mixing,[5] and Raman lasing.[6] Utilization of these appealing features has resulted in myriad applications including low threshold lasers,[7] frequency comb generators,[8] and extremely sensitive biological sensors.[9] However, spherical WGM resonators have limited functionality due to the restriction of their on-chip integration by shape and a priori unknown eccentricity. Resonators with a definite state of eccentricity can be obtained by deforming a sphere between two solid plates, compromising spherical symmetry.[10] A current state-of-the-art technology is the toroidal silica microresonator, produced by lithography and high power laser reflow techniques, which seem to have an advantage for mass production and on-chip integration. Unfortunately, the production demands individual surface reflow for each and every resonator with high temperatures (above 1000 °C), hindering the integration of other optical components on the same substrate.[11] In addition, using silica as a resonator material makes optical coupling to an on-chip high refractive index waveguide highly inefficient. Alternatively, chalcogenides have recently been considered as a material for active and passive resonant media because of their high refractive index ($n = 2.2$–3.4), wide mid-IR transparency window, extraordinary high nonlinearity, photosensitivity, low two-photon absorption, low phonon energy, and ability to be doped by most of the rare earth elements.[12,13] Even though their Q-factors ($<7 \times 10^7$) are not as high as that of silica WGM resonators, thresholds for some nonlinear optical interactions are on the same order of magnitude, due to their high nonlinearity.[14] Nevertheless, similar obstacles exist before the full utilization of the chalcogenide microresonators, emerging from the exclusive nature of their production and integration phases. Methods compatible to mass production can produce hundreds of polydisperse spheres.[15,16] However, spheres with a desired shape and optical quality need to be separated from the debris by very elaborate and laborious techniques, and manipulated by their attachment on a fiber tip[17] or using optical tweezers.[18] Other methods, similar to production of silica spheres, rely on melting the tip of a chalcogenide fiber by laser heating.[19] Although these spheres are attached to a fiber stem, allowing them to be easily manipulated, high yield production is not possible due to the very nature of the process and the eccentricity caused by the stem.[20] Besides spheres on a fiber tip, an additional example for the in-situ formation of WGM resonators is photoinduced microcavity resonators in chalcogenide microfibers.[21,22] The integration of a single chalcogenide sphere coupled to a tapered fiber has been demonstrated by packaging the system using a UV-curable polymer.[23] Another route towards the production of chalcogenide microspheres is to induce the Plateau-Rayleigh (PR) capillary instability[24,25] in a chalcogenide fiber, which was first shown by optical fusing the bare core in the midair[16] and recently in a polymer cladding for small fiber lengths (<1 mm) by using a tapering process[26] and a local heat treatment.[27]

Here, we report a novel versatile method for the high yield production and on-chip integration of self-assembled globally oriented high-Q WGM chalcogenide microresonators with surface-tension-induced spherical, spheroidal, and ellipsoidal boundaries with sub-nanometer roughness. The production involves the formation of chalcogenide microspheres within a polymer fiber of extensive length (≥ 5 cm), which was accomplished by preserving the integrity of the polymer cladding during thermal treatment. The transformation of these spherically symmetric resonators en masse into axisymmetric or asymmetric resonators was conducted by controlled plastic deformation. By using a special polymer as an adhesive layer in the integration phase, we demonstrate the near-perfect transfer and attachment of the microresonators embedded

O. Aktas, E. Ozgur, Dr. O. Tobail, M. Kanik,
E. Huseyinoglu, Prof. M. Bayindir
UNAM-National Nanotechnology Research Center
Bilkent University
06800, Ankara, Turkey
E-mail: bayindir@nano.org.tr
E. Ozgur, M. Kanik, E. Huseyinoglu, Prof. M. Bayindir
Institute of Materials Science and Nanotechnology
Bilkent University
06800, Ankara, Turkey
O. Aktas, Prof. M. Bayindir
Department of Physics
Bilkent University
06800, Ankara, Turkey
Dr. O. Tobail
Egypt Nanotechnology Center
Cairo University
12588, Giza, Egypt

www.MaterialsViews.com

ADVANCED
OPTICAL
MATERIALS
www.advopticalmat.de

COMMUNICATION

in the polymer fiber on any substrate, preserving their initial symmetries. As a result, novel on-chip chalcogenide WGM resonators are introduced to the WGM microresonator family. By optical characterization of the spherical and spheroidal microresonators, we routinely obtain very high Q-factors: up to $Q_L = 3.1 \times 10^5$ which is, to our knowledge, the highest loaded Q-factor ever measured in As_2Se_3 WGM microresonators evanescently coupled to a silica tapered fiber.

For the production of chalcogenide WGM microresonators, multimaterial fibers, which consist of a chalcogenide glass (As_2Se_3) core and a thermoplastic polymer polyethersulfone (PES) cladding, were used in this study. Fibers were obtained as a result of the size reduction of a preform (see Figure S1a) by thermal drawing in a fiber tower (see Figure S1b). The amorphous As_2Se_3 rod used in the production of the preform was prepared from high purity As and Se elements using a sealed-ampule melt-quenching technique (see the Supporting Information).[28] As a result of fiber drawing, we obtained fibers (see Figure S1c) with different diameters, d, ranging from 1 mm to 30 μm, corresponding to As_2Se_3 core diameters ranging from 200 μm to 6 μm. In order to produce a long chain of uniform As_2Se_3 microspheres embedded in a PES fiber, we developed a novel thermal treatment technique, which is based on extensive convective radial heating of the fiber with a conformal polymer cover preserving the integrity and straightness of the cladding at elevated temperatures (see Figure S2). A long uncovered fiber with free ends on a hot plate was observed to be bent or even twisted while releasing the built-in tension originating from the thermal drawing process.

On the contrary to the processing conditions to which a fiber is exposed during fiber drawing, such as sudden cooling under tension, thermal treatment of As_2Se_3 core PES cladding fiber at elevated temperatures (260–310 °C) for substantial times leads ultimately to break-up of the continuous core into a chain of self-assembled spheres and inter-sphere satellites, due to overwhelming of surface tension against viscous forces. In order to understand the dynamics of PR instability and the evolution of the fiber core, we conducted finite element simulations (see the Supporting Information) by using temperature dependent viscosities for both materials (see Figure S3). Simulation and experimental snapshots of in-fiber microsphere formation (**Figure 1**a,b) reveal that amplitude of the dominant sinusoidal modulation on the core surface grows over time until pinch-off, at which point detachment occurs, leaving a smaller structure in the middle exposed to the same instability over and over again, resulting in a fractal pattern of main spheres with satellite spheres on their sides (Movie S1 and Movie S2). Satellite and sub-satellite sphere formations can be observed down to the 5th generation, where the fractal process eventually stops reaching submicrometer scales (see Figure S4). Instability wavelengths, which are spatial periods of the structural perturbations on the fiber surface, determining the separation between the largest spheres at fiber core break-up, are given as a function of temperature along with the experimental and theoretical comparisons, and characteristic times for core break-up are given in Figure S5 and Figure S6, respectively. Pre-compensating the fiber diameter or adjusting the ratio of core diameter to outer diameter, a wide range of sphere sizes (1 mm–1 μm) can be obtained. Fibers enclosing spherical
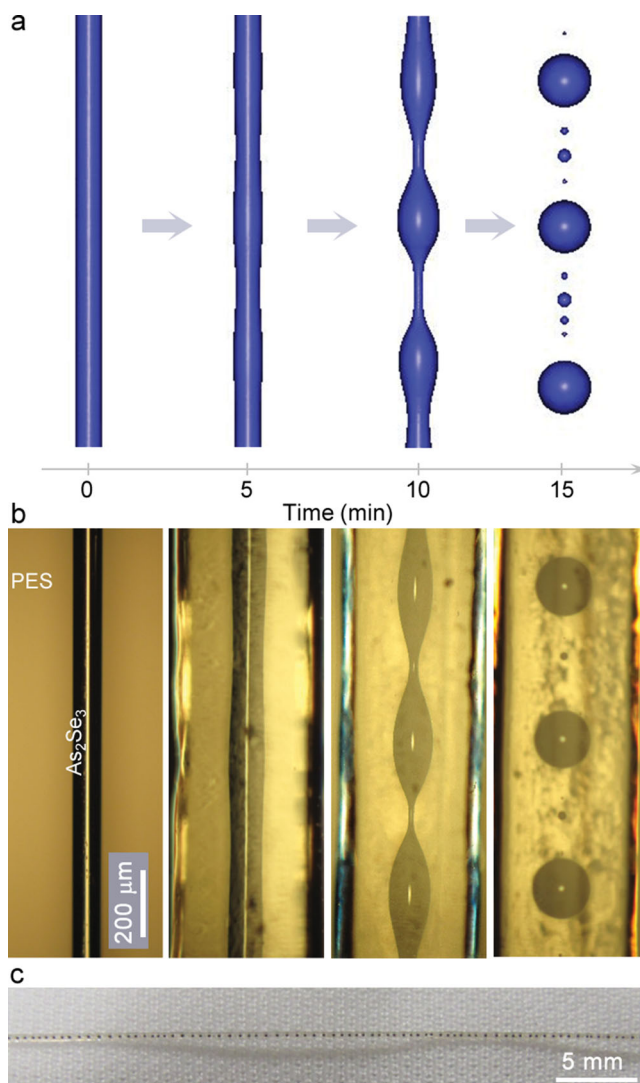
Figure 1. Simulation and experimental snapshots showing the evolution of microsphere formation in the As_2Se_3 core of a PES cladding fiber by Plateau-Rayleigh (PR) instability. (a) A finite element fluid dynamics simulation discloses the dynamics of PR instability occurring in the fiber. (b) Initially intact 80 μm diameter chalcogenide core of the polymer cladding fiber turns into a self-assembled chain of 160 μm diameter spheres and smaller satellite spheres embedded inside the fiber, in 15 min at 300 °C. (c) A photograph of a 5 cm long PES cladding fiber with embedded As_2Se_3 microspheres.

microresonators were produced as long as 5 cm in length, as shown in Figure 1c, limited only by the length of the tubular oven. However, uneven distribution of temperature or of stress caused by the conformal cover can result in unequal separations between main spheres.

Using continuous volume preserving transformations of the spherical microresonators induced by controlled plastic deformations in a custom made setup, we produced 3D ellipsoidal asymmetric resonant cavities (ARCs) with arbitrary eccentricity. ARCs, intrinsically possessing emission directionality, are important for laser applications[29] as well as for fundamental studies of classical and quantum chaos, due to the resemblance between the Hamiltonian dynamics of a point mass moving

in a 3D space constrained by hard walls, and the ray dynamics of the light in a uniform dielectric cavity.[30] Also, recently, enhanced energy storage in deformed optical resonators was reported.[31]
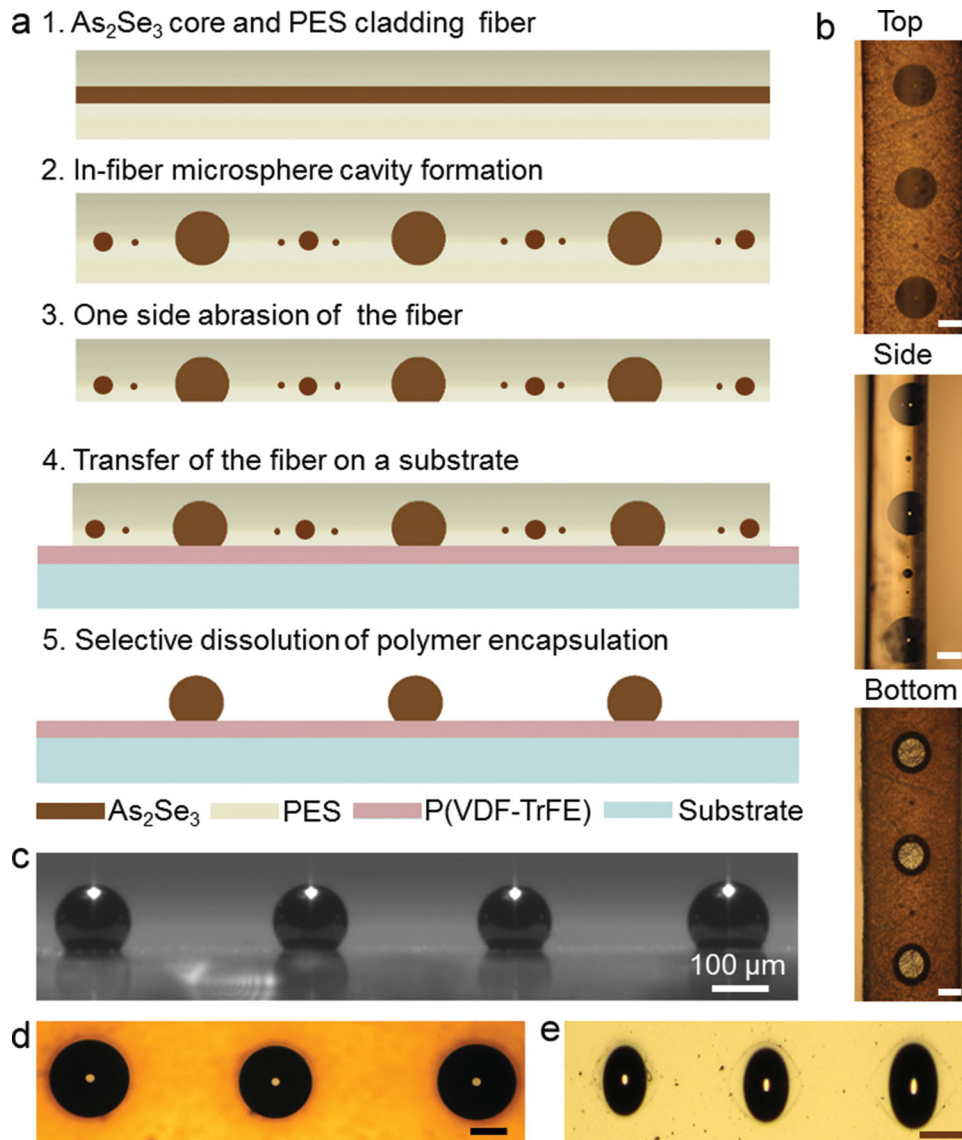
Mechanical deformation of a PES polymer fiber enclosing an As_2Se_3 microsphere array between two parallel glass plates at a temperature of 280 °C, which is above the glass transitions of the As_2Se_3 (T_g = 170 °C) and PES (T_g = 220 °C), transforms the array of spheres into an array of triaxial ellipsoids, and finally into an array of "cigar-shaped" bodies globally oriented in a perpendicular direction to the fiber axis, because the fiber yields readily in this direction. Schematics of the fiber deformation process between two parallel glass plates in a high temperature furnace and deformation setup can be seen in **Figure 2**a and Figure S7, respectively. Optical reflection micrographs of deformed fibers can be seen in Figure 2b–d. The specular Fresnel reflection (R = 22%) from the surface of resonators can be used to easily discriminate spherical and ellipsoidal cavities. We used dichloromethane (DCM) to dissolve PES cladding and to reveal spherical, ellipsoidal and "cigar-shape" cavities. Scanning electron microscopy (SEM) micrographs of the resonators given in Figure 2e–g show that it is possible to obtain smooth surfaces after deformations in a polymer encapsulation. SEM micrographs in Figure 2h,i show profile views of ellipsoidal and "cigar shape" cavities. Furthermore, we conducted atomic force microscopy measurements for the quantitative surface characterization of the microresonators. Sub-nanometer *rms* surface roughness (σ < 0.6 nm) was found from a 500 nm × 500 nm surface scan on top polar region of an ellipsoid (see Figure 2j).

High yield production of spherical and ellipsoidal resonators inherently ordered in a polymer encapsulation can provide a unique advantage for multiple uses of these microresonators in photonics circuits, which is a critical barrier impeding their further development for relevant applications. Exploiting this advantage, we developed a method enabling on-chip integration of the chalcogenide microresonators with various shapes and sizes (see **Figure 3**a). In this method, the integration process involves two steps, which are the preparation of the substrate and the fiber encapsulation of an array of microresonators. We used 100 μm thick glass coverslips as substrates, though there is no restriction for the substrate material. The substrates were spin coated with poly(vinylidenefluoride-*co*-trifluoroethylene) P(VDF-*co*-TrFE) (see

Experimental Section). After numerous trials with different polymers, P(VDF-*co*-TrFE) was found to be the most convenient as an adhesion layer regarding its low glass transition temperature (T_g = 80 °C), high adhesive forces towards chalcogenides, and
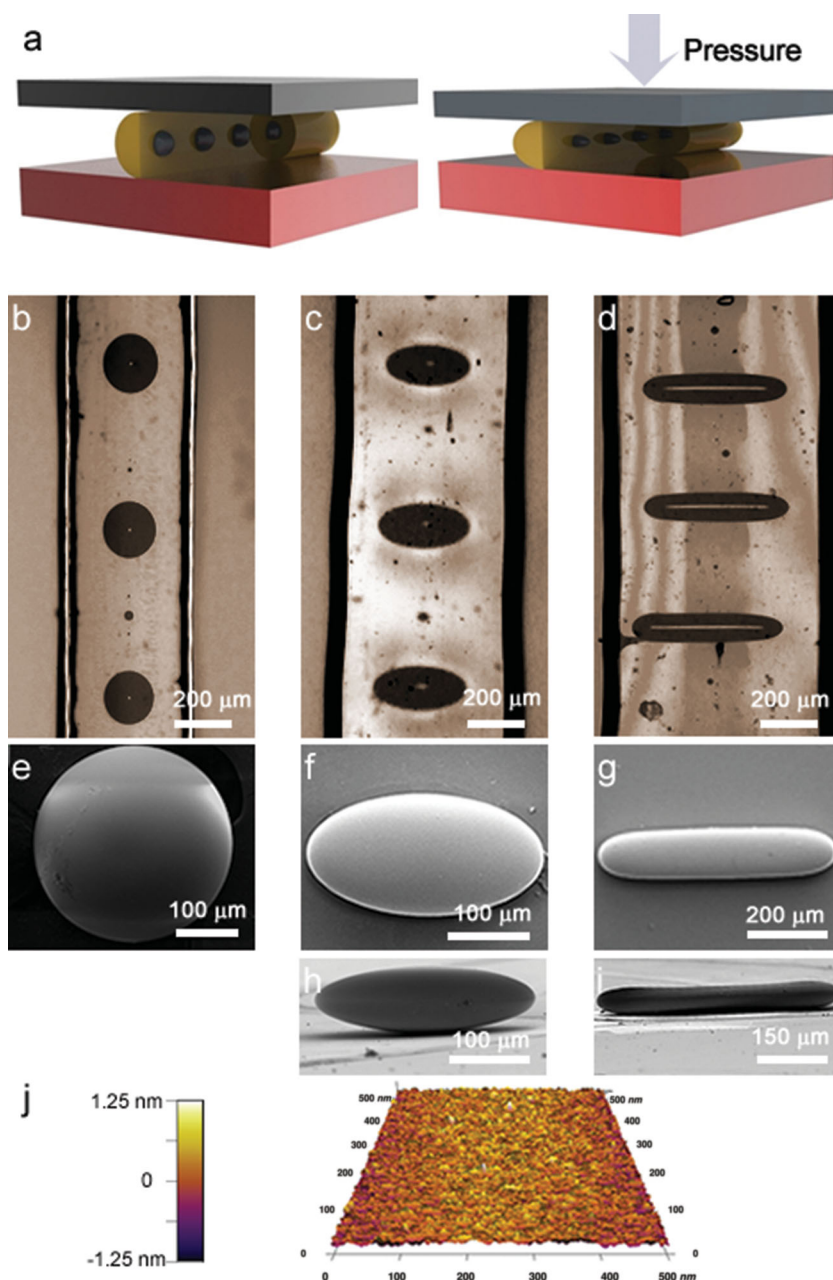
Figure 2. High yield production of 3D asymmetric microresonators via continuous volume preserving transformations induced by controlled plastic deformations. (a) Schematics of fiber deformation between two parallel glass plates in a high temperature furnace. Mechanical deformation of a PES polymer fiber enclosing an As_2Se_3 microsphere array at a temperature above the T_g of the both materials, transforms (b) the array of spheres into (c) an array of triaxial ellipsoids, then into (d) an array of "cigar-shaped" bodies globally oriented in perpendicular direction to the fiber axis. SEM micrographs show (e) spherical, (f) ellipsoidal, and (g) "cigar-shape" cavities extracted out by dissolving the PES polymer cladding in DCM. SEM micrographs show (h) ellipsoidal and (i) "cigar-shape" cavities in profile view. (j) AFM surface characterization of an ellipsoidal microresonator on (500 nm × 500 nm) top polar region shows sub-nanometer rms surface roughness (σ < 0.6 nm).

www.MaterialsViews.com

ADVANCED
OPTICAL
MATERIALS
www.advopticalmat.de

COMMUNICATION

Figure 3. High yield production and on-chip integration of chalcogenide WGM microresonators on an arbitrary substrate. (a) The process starts with fabrication of As$_2$Se$_3$ core PES cladding fibers by thermal drawing. Then, in-fiber microsphere formation is induced by PR instability at elevated temperatures. As a third step, partial abrasion of the fiber cladding is achieved by a simple sandpapering process, exposing bottom sides of the spheres as contact surfaces for adhesion. In the fourth step, the resulting fiber is transferred manually onto a substrate spin coated with P(VDF-co-TrFE) and then heated to promote adhesion up to 210 °C, which is below the T_g of PES cladding but above the T_g of both As$_2$Se$_3$ core and the P(VDF-co-TrFE) coating. At the last step, the largest microcavities attached to the surface can be released from the encapsulating PES polymer by selective dissolution in DCM, which has minimal effect on the substrate polymer coating. All satellite spheres are also flushed away spontaneously by the dissolution process. Optical micrographs show the (b) top, side and bottom views of the fiber after sandpapering one of its sides, (c) on-chip spherical chalcogenide microresonator array, (d) spherical microresonators directly integrated on the gold coated surface without any polymer coating, and (e) ellipsoidal microresonators integrated on P(VDF-co-TrFE) polymer coated surface. All scale bars are 100 μm.

chemical resistance against DCM. As for the preparation of the fiber, partial abrasion of the cladding was achieved by a simple sandpapering process (see Experimental Section), exposing the bottoms of the embedded microspheres as contact surfaces for adhesion. Optical micrographs of top, side, and bottom views of the fiber after sandpapering operation can be seen in Figure 3b. The resulting fiber was transferred manually onto the substrate spin coated with a P(VDF-co-TrFE) polymer and then heated to promote adhesion up to a temperature of 210 °C, which is below the T_g of the PES cladding, but above the T_g of the As$_2$Se$_3$ core

and the P(VDF-co-TrFE) coating. Finally, microresonators with their bottoms attached to the substrate surface were revealed by selective dissolution of the encapsulating PES polymer in DCM (see Experimental Section). During the dissolution process all satellite cavities, which are smaller than the main cavities, are also flushed away spontaneously. This integration method enables the transfer of cavities on any substrate without any shape distortion, preserving the initial symmetry, due to protection by rigid PES encapsulation. An optical micrograph of on-chip well-ordered spherical chalcogenide WGM microresonator can

COMMUNICATION

be seen in Figure 3c. Integration of spherical microresonators directly onto the metal surfaces is also possible (see Figure 3d); however, it requires temperatures higher than the T_g of PES, which is not suitable for non-spherical cavities due to the softening of PES encapsulation, and surface tension compromising the non-spherical symmetry at elevated temperatures. Ellipsoidal microresonators integrated on a P(VDF-co-TrFE) polymer coated surface can be also seen in Figure 3e. Energy dispersive X-ray spectroscopy (EDX) results obtained from the surfaces of on-chip microsphere resonators demonstrate the consistence of the atomic ratio of As_2Se_3 (see Figure S8), besides showing that no impurity or residual polymer exists on the surfaces of microspheres after the dissolution process.

Another microcavity type with a different symmetry can be produced by compressing the on-chip microspheres upside down on a hot plate after their integration. Because of the different boundary conditions compared to those inside a polymer fiber, axisymmetric plastic deformation is favorable in this case and spheroidal microresonators with arbitrary elliptic cross sections can be easily produced. SEM micrographs of on-chip spherical/spheroidal/ellipsoidal chalcogenide WGM microresonator arrays are shown in **Figure 4**a–c.

We used tapered silica fibers (see the Supporting Information) with submicrometer waist diameters (~700 nm) to evanescently couple light into these resonators and to capture transmission mode spectra (**Figure 5**a–d). Schematics of the experimental setup used for optical characterizations of microresonators is given in Figure S9. In order to eliminate thermo-optic effects (see Figure S10), we used very low optical input powers (~100 nW). Wavelength scanning ranges of the external cavity laser were set as 12 nm and 50 pm for the
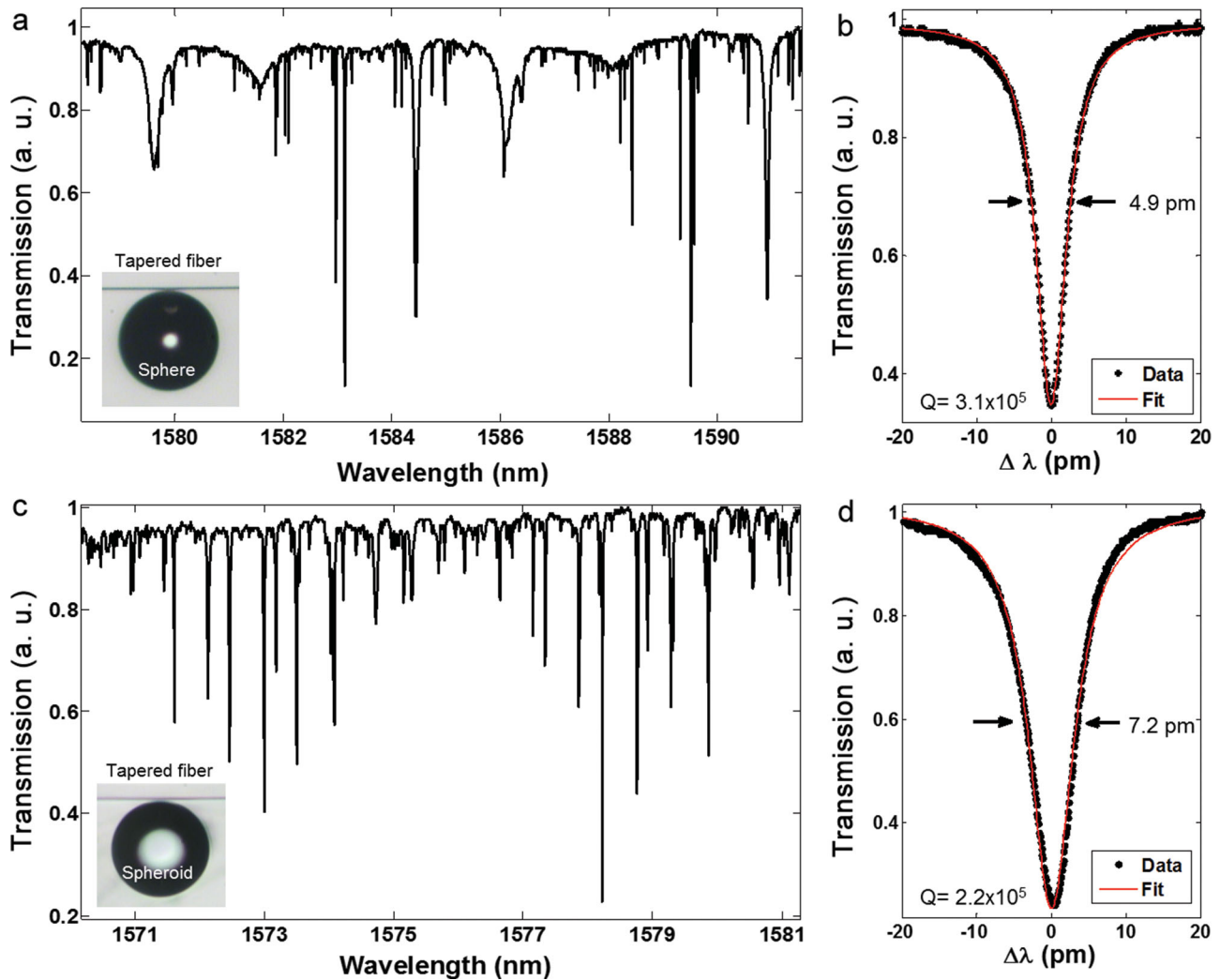
acquisition of two free spectral range (FSR) wide spectra and single mode wide spectra, respectively. An adjustable polarization controller was used to maximize optical coupling into TE modes.

Despite the refractive index mismatch between the silica tapered fiber ($n = 1.44$) and the chalcogenide microresonators ($n = 2.83$) in the wavelength range of interest, it was possible to observe optical couplings to spherical and spheroidal microresonators, facilitated by a tapered silica fiber with sub-micrometer waist diameter, and resonators with small radii (~25 μm). The strength of the optical coupling critically depends on two parameters: the amount of field overlap, and phase matching between the fiber modes and the WGMs.[32] Excitation of modes with high radial mode numbers are more favorable than low order modes in our case, because high order radial modes have low propagation constants, reducing phase mismatch, and higher evanescent field fraction outside the cavity, enhancing the field overlap (see the Supporting Information, including Figure S11). Reducing the size of the cavities also enhances optical coupling, which is in accordance with our experiments on microresonators under 60 μm in diameter. We observed a series of resonance dips corresponding to WGMs of a microsphere ($D = 50$ μm) and an oblate microspheroid ($D = 57$ μm) with transmissions as low as 10 dB. Resonance mode splitting can also be seen in the spectra of a microspheroid (see Figure 5c), because of the broken degeneracy of azimuthal modes. In single mode spectra, a full width at half maximum value (FWHM) of 4.9 pm was obtained by a Lorentzian fit to the resonance mode of the microsphere at 1551.858 nm, corresponding to a loaded quality factor of $Q_L = 3.1 \times 10^5$ associated with a transmission depth of $K = 4.6$ dB (see Figure 5b). The average of the loaded quality
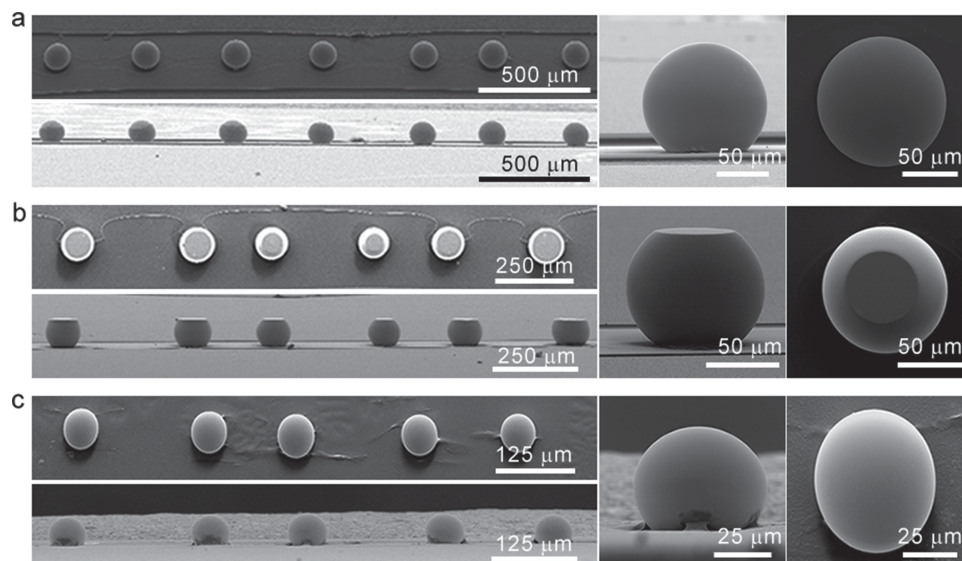
Figure 4. SEM micrographs of on-chip spherical/spheroidal/ellipsoidal chalcogenide microresonator arrays. Close-ups of some individual resonators in top and profile perspectives, show quality of production and on-chip integration such as the alignment of characteristic features (like equator plane), eccentricity, smoothness, and cleanliness of the resonator surfaces. (a) Top and profile SEM micrographs of spherical As_2Se_3 microresonator array and a single microsphere. Average diameter of spheres is $d_{ave} = 124.4$ μm with standard deviation $\sigma = 3.4$ μm (2.7%). As can be seen in the profile of the resonator, transfer and integration of the microsphere is accomplished with a very low aspherical deformation, and a good degree of parallel alignment of the equator plane with respect to the substrate surface. Top and profile SEM micrographs of (b) a spheroidal As_2Se_3 microresonator array and a single microspheroid, and (c) an ellipsoidal As_2Se_3 microresonator array and a single microellipsoid.

Materials
Views
www.MaterialsViews.com

ADVANCED
OPTICAL
MATERIALS
www.advopticalmat.de

COMMUNICATION

Figure 5. Optical characterizations of on-chip spherical and spheroidal chalcogenide microresonators. (a) Transmission spectra of an As$_2$Se$_3$ microsphere resonator of 50 µm in diameter. Coupling strength of resonance modes can be as high as 10 dB. FSR is 6.39 nm. (b) Lorentzian fit to a resonance dip at 1551.858 nm shows that the FWHM and loaded quality factor Q_L of the resonance mode are 4.9 pm and 3.1 × 10^5, respectively. Inset shows evanescent coupling of light into the microsphere resonator using a tapered silica fiber with a sub-micrometer waist diameter. (c) Transmission spectra of an As$_2$Se$_3$ microspheroid resonator of 57 µm in equator diameter. FSR is 5.22 nm. (d) Lorentzian fit to a resonance dip at 1571.589 nm shows that FWHM and loaded quality factor Q_L of resonance mode are 7.2 pm and 2.2 × 10^5, respectively. Inset shows evanescent coupling of light into the microspheroid resonator using a tapered silica fiber.

factors we measured is $Q_{ave} = 2.9 \times 10^5$ with a standard deviation of $\sigma = 0.6 \times 10^5$. Similarly, a FWHM of 7.2 pm was obtained by a Lorentzian fit to the resonance mode of the microspheroid at 1571.589 nm, corresponding to a loaded quality factor of $Q_L = 2.2 \times 10^5$, associated with a transmission depth of $K = 6.2$ dB (see Figure 5d). The maximum Q-factor reported for As$_2$Se$_3$ WGM resonators is $Q_{max} = 2.3 \times 10^6$, which was measured using a phase matched silicon waveguide evanescently coupled to a microsphere produced on the tip of a fiber.[19]

Experimentally measured quality factors Q_L are described by the expression

$$1/Q_L = 1/Q_O + 1/Q_c \qquad (1)$$

written in terms of intrinsic Q_0 and extrinsic Q_c quality factors, which are determined by resonator related losses and coupling

losses, respectively. The intrinsic quality factor of WGM modes of microresonators $Q_0^{-1} = Q_{rad}^{-1} + Q_{ss}^{-1} + Q_{mat}^{-1}$ are determined by several factors such as radiative losses Q_{rad}^{-1}, scattering losses Q_{ss}^{-1}, due to surface roughness and contamination, and material absorption losses Q_{mat}^{-1}. For intermediate size resonators ($D \sim 50$ µm) with sub-nanometer surface roughness ($\sigma < 0.6$ nm) as in our case, and in the absence of surface contaminants, Q-factor is only limited by material losses and given as[33]

$$Q_{mat} = 2\pi n / \alpha\lambda \qquad (2)$$

where α is absorption coefficient, n is refractive index and λ is wavelength. Using a material absorption coefficient $\alpha = 1.6$ m^{-1} of a commercially available As$_2$Se$_3$ glass at 1550 nm (see the Supporting Information including Figure S12a), the absorption limited intrinsic Q-factor was found to be

ADVANCED
OPTICAL
MATERIALS
www.advopticalmat.de

Materials
Views
www.MaterialsViews.com

COMMUNICATION

$Q_{mat} = 7.2 \times 10^6$, which is the maximum limit for experimentally obtainable quality factors (see Figure S12b). In addition, all WGM modes of the cavity suffer from the optical coupling process as well. The amount of coupling loss depends on phase matching and the field overlap of modes determined by mode order, radius of the cavity, radius of the tapered fiber, and the air gap between them.[34] By adjusting the air gap, the quality factor Q_c set by coupling loss can be tuned to achieve different regimes of coupling, where transmission T drops to zero ($K = 1$) at critical coupling. Using the measured loaded quality factor $Q_L = 3.1 \times 10^5$ and the transmission depth $K = 0.65$ in the following derived expression,[35]

$$Q_0 = 2Q_L[1+\sqrt{1-K}]/K \qquad (3)$$

we calculated the intrinsic quality factor as $Q_0 = 0.76 \times 10^6$, corresponding to an absorption coefficient $\alpha = 15$ m^{-1}. It can be considered to be on the order of magnitude of absorption limited quality factor Q_{mat} of As$_2$Se$_3$. The discrepancy is assumed to be caused by a higher optical absorption in our synthesized chalcogenide glass or water condensing on cavity surfaces in lab conditions, at which we observed one order of magnitude degradation in the Q-factors of chalcogenide microresonators held three weeks in lab conditions.

We could not detect any transmission dips in the mode spectrum of triaxial ellipsoids with tapered silica fibers favoring only coupling to high order modes; however, we can directly observe light coupling into the micro-ellipsoids by thermal imaging (see Movie S3). The reason for the absence of transmission dips in the spectrum of ellipsoids could be due to the expected complete suppression of high order modes in deformed resonators of high eccentricity[36] or some mechanisms similar to Arnold diffusion in the phase space of 3D ARCs, resulting in Q-spoiling with refractive escape of light,[37] which require further theoretical studies of ARCs in 3D. Nevertheless, phase matched waveguides can be used to couple light evanescently into low order modes of ellipsoidal microresonators to observe transmission dips.

In summary, we have developed a simple, scalable, and lithography-free method for the production and on-chip integration of high-Q factor WGM chalcogenide microresonators with spherical, spheroidal, and ellipsoidal boundaries with sub-nanometer surface roughness. High yield, low cost production of hundreds of self-assembled chalcogenide microresonators was achieved inducing PR instability in extended lengths of a multimaterial fiber. Since PR instability is a well-established phenomenon, our production and on-chip integration scheme are not limited to As$_2$Se$_3$ and can be applied to other important optical materials including As$_2$S$_3$, Si, Ge, and SiO$_2$, which can be turned into microcavities inside suitable cladding materials.[38–40] Furthermore, active chalcogenide resonators can be made by doping with rare earth elements for on-chip laser applications. Utilizing the shape preserving protection of the polymer encapsulation, near-perfect transfer of the embedded microresonators onto any substrate in a globally oriented fashion is demonstrated. We observed loaded Q-factors as high as $Q_L = 3.1 \times 10^5$ in our on-chip microcavity resonators. To our knowledge, it is the highest Q-factor ever measured in As$_2$Se$_3$ microresonators with silica tapered fibers favoring optical coupling only to high order WGM modes. Easy on-chip integration of highly nonlinear high-Q microresonators can pave the way for new or extended exploitation of photonic devices in applications such as mid-IR sensors for the detection of molecular fingerprints, frequency comb generators for the generation of ultra-pure microwaves, ultra-low threshold microlasers with emission directionality, electro-optical tunable filters or modulators for optical communications, and optical logic gates for all-optical processors.

Experimental Section

Spin Coating of the Substrates: Before the integration of microresonators, substrates were spin coated with P(VDF-*co*-TrFE) solution for 45 s at 6500 rpm. The solution was prepared by sonification of P(VDF-*co*-TrFE) (30 g) in dimethylformamide (50 mL). Substrates were then placed on a hotplate at 100 °C for 1 h to accelerate solvent evaporation.

Sandpapering of Fibers: To facilitate sandpapering process, fibers were attached to glass plate with double sided bands, then exposed parts of the fibers were rubbed against sheets of SiC sandpapers with size of abrasive particles decreasing from 5 µm to 1 µm. After sandpapering process, fibers were released from the glass plate and cleaned by sonification in isopropyl alcohol for 10 min.

Dissolution of PES Encapsulation: In order to remove the PES encapsulation of the microresonators integrated onto a substrate, we flushed the substrate with fresh DCM until most of the PES cladding dissolved away, then the substrate was placed in a fresh DCM solution for 1 h, and finally flushed over with fresh DCM again to remove dissolved polymer residues. As a final treatment, substrate with integrated microresonators was placed in a vacuum oven at 50 °C for 2 h to evaporate residual DCM.

Supporting Information

Supporting Information is available from the Wiley Online Library or from the author.

Acknowledgements

[1] K. J. Vahala, *Nature* **2003**, *424*, 839.
[2] V. B. Braginsky, M. L. Gorodetsky, V. S. Ilchenko, *Phys. Lett. A* **1989**, *137*, 393.
[3] D. K. Armani, T. J. Kippenberg, S. M. Spillane, K. J. Vahala, *Nature* **2003**, *421*, 925.

[4] T. Carmon, K. J. Vahala, *Nat. Phys.* **2007**, *3*, 430.

[5] P. Del'Haye, A. Schliesser, O. Arcizet, T. Wilken, R. Holzwarth, T. J. Kippenberg, *Nature* **2007**, *450*, 1214.

[6] S. M. Spillane, T. J. Kippenberg, K. J. Vahala, *Nature* **2002**, *415*, 621.

[7] V. Sandoghdar, F. Treussart, J. Hare, V. Lefevre-Seguin, J.-M. Raimond, S. Haroche, *Phys. Rev. A* **1996**, *54*, R1777.

[8] T. J. Kippenberg, R. Holzwarth, S. A. Diddams, *Science* **2011**, *332*, 555.

[9] F. Vollmer, S. Arnold, D. Keng, *Proc. Natl. Acad. Sci. USA* **2008**, *105*, 20701.

[10] G. S. Murugan, J. S. Wilkinson, M. N. Zervas, *Appl. Phys. Lett.* **2012**, *101*, 071106.

[11] M. Hossein-Zadeh, K. J. Vahala, *Opt. Exp.* **2007**, *15*, 166.

[12] B. J. Eggleton, B. Luther-Davies, K. Richardson, *Nat. Photon.* **2011**, *5*, 141.

[13] V. G. Ta'eed, N. J. Baker, L. Fu, K. Finsterbusch, M. R. E. Lamont, D. J. Moss, H. C. Nguyen, B. J. Eggleton, D. Y. Choi, S. Madden, B. Luther-Davies, *Opt. Exp.* **2007**, *15*, 9205.

[14] F. Vanier, M. Rochette, N. Godbout, Y.-A. Peter, *Opt. Lett.* **2013**, *38*, 4966.

[15] G. R. Elliott, D. W. Hewak, G. S. Murugan, J. S. Wilkinson, *Opt. Exp.* **2007**, *15*, 17452.

[16] C. Grillet, S. N. Bian, E. C. Magi, B. J. Eggleton, *Appl. Phys. Lett.* **2008**, *92*, 171109.

[17] G. R. Elliott, G. S. Murugan, J. S. Wilkinson, M. N. Zervas, D. W. Hewak, *Opt. Exp.* **2010**, *18*, 26720.

[18] L. Zhang, Y.-X. Wang, F. Zhang, R. O. Claus, *J. Opt. Soc. Am. B* **2006**, *23*, 1793.

[19] D. H. Broaddus, M. A. Foster, I. H. Agha, J. T. Robinson, M. Lipson, A. L. Gaeta, *Opt. Exp.* **2009**, *17*, 5998.

[20] A. Mazzei, S. Gotzinger, L. de S. Menezes, V. Sandoghdar, O. Benson, *Opt. Commun.* **2005**, *250*, 428.

[21] A. L. Watts, N. Singh, C. G. Poulton, E. C. Magi, I. V. Kabakova, D. D. Hudson, B. J. Eggleton, *J. Opt. Soc. Am. B* **2013**, *30*, 3249.

[22] F. Luan, E. Magi, T. Gong, I. Kabakova, B. J. Eggleton, *Opt. Lett.* **2011**, *36*, 4761.

[23] P. Wang, M. Ding, T. Lee, G. S. Murugan, L. Bo, Y. Semenova, Q. Wu, D. Hewak, G. Brambilla, G. Farrell, *Appl. Phys. Lett.* **2013**, *102*, 131110.

[24] S. Tomotika, *Proc. R. Soc. Lond. A* **1935**, *150*, 322.

[25] L. Rayleigh, *Proc. R. Soc. Lond.* **1879**, *29*, 71.

[26] S. Shabahang, J. J. Kaufman, D. S. Deng, A. F. Abouraddy, *Appl. Phys. Lett.* **2011**, *99*, 161909.

[27] J. J. Kaufman, G. Tao, S. Shabahang, E.-H. Banaei, D. S. Deng, X. Liang, S. G. Johnson, Y. Fink, A. F. Abouraddy, *Nature* **2012**, *487*, 463.

[28] A. F. Abouraddy, O. Shapira, M. Bayindir, J. Arnold, F. Sorin, D. S. Hinczewski, J. D. Joannopoulos, Y. Fink, *Nat. Mater.* **2006**, *5*, 532.

[29] X.-F. Jiang, Y.-F. Xiao, C.-L. Zou, L. He, C.-H. Dong, B.-B. Li, Y. Li, F.-W. Sun, L. Yang, Q. Gong, *Adv. Mater.* **2012**, *24*, OP260.

[30] J. U. Nockel, A. D. Stone, *Nature* **1997**, *385*, 45.

[31] C. Liu, A. D. Falco, D. Molinari, Y. Khan, B. S. Ooi, T. F. Krauss, A. Fratalocchi, *Nat. Photon.* **2013**, *7*, 473.

[32] M. J. Humphrey, E. Dale, A. T. Rosenberger, D. K. Bandy, *Opt. Commun.* **2007**, *271*, 124.

[33] M. L. Gorodetsky, A. A. Savchenkov, V. S. Ilchenko, *Opt. Lett.* **1996**, *21*, 453.

[34] C.-L Zou, Y. Yang, C.-H. Dong, Y.-F. Xiao, X.-W. Wu, Z.-F. Han, G.-C. Guo, *J. Opt. Soc. Am. B* **2008**, *25*, 1895.

[35] M. L. Gorodetsky, V. S. Ilchenko, *J. Opt. Soc. Am. B* **1999**, *16*, 147.

[36] V. S. Ilchenko, M. L. Gorodetsky, X. S. Yao, L. Maleki, *Opt. Lett.* **2001**, *26*, 256.

[37] S. Lacey, H. Wang, D. H. Foster, J. U. Nockel, *Phys. Rev. Lett.* **2003**, *91*, 033902.

[38] J. Ballato, T. Hawkins, P. Foy, R. Stolen, B. Kokuoz, M. Ellison, C. McMillen, J. Reppert, A. M. Rao, M. Daw, S. Sharma, R. Shori, O. Stafsudd, R. R. Rice, D. R. Powers, *Opt. Express* **2008**, *16*, 18675.

[39] P. Wang, T. Lee, M. Ding, A. Dhar, T. Hawkins, P. Foy, Y. Semenova, Q. Wu, J. Sahu, G. Farrell, J. Ballato, and G. Brambilla, *Opt. Lett.* **2012**, *37*, 728.

[40] A. Gumennik, L. Wei, G. Lestoquoy, A. M. Stolyarov, X. Jia, P. H. Rekemeyer, M. J. Smith, X. Liang, B. J.-B. Grena, S. G. Johnson, S. Gradecak, A. F. Abouraddy, J. D. Joannopoulos, Y. Fink, *Nat. Commun.* **2013**, *4*, 2216.

SUPPORTING INFORMATION

A New Route of Fabricating On-Chip Chalcogenide Microcavity Resonator Array

By *Ozan Aktas, Erol Ozgur, Osama Tobail, Mehmet Kanik, Ersin Huseyinoglu and Mehmet Bayindir**

Prof. M. Bayindir, O. Aktas, E. Ozgur, Dr. O. Tobail, M. Kanik and E. Huseyinoglu
UNAM-National Nanotechnology Research Center, Bilkent University, 06800 Ankara, Turkey
E-mail: bayindir@nano.org.tr

Prof. M. Bayindir, E. Ozgur, M. Kanik and E. Huseyinoglu
Institute of Materials Science and Nanotechnology, Bilkent University, 06800 Ankara, Turkey

Prof. M. Bayindir and O. Aktas
Department of Physics, Bilkent University, 06800 Ankara, Turkey

Dr. O. Tobail
Egypt Nanotechnology Center, Cairo University, 12588 Giza, Egypt

Table of Contents

Experimental Details

Glass Synthesis: The amorphous As_2Se_3 rod used in fiber drawing was prepared from high purity As and Se elements (Sigma Aldrich) using sealed-ampule melt-quenching technique. The materials As (wt% 40) and Se (wt% 60) were placed into a quartz tube under nitrogen atmosphere. In order to remove surface oxides and impurities, the tube was heated above 300 ºC under vacuum condition. After the tube was cooled down to room temperature, it was sealed under $\sim 10^{-3}$ Torr vacuum. The sealed tube was placed in a rocking oven and heated up to 800 ºC at a rate of 2 ºC.min^{-1}. After the oven was held at this temperature at vertical position for 24 hours, it was rocked at least for 6 hours to increase homogeneity. Subsequently, oven was cooled down to 600 ºC and the tube was quenched in water to form As_2Se_3 intermetallic glass rod with 10 cm length and 6 mm diameter.

Fiber Tapering: Single mode silica fibers were tapered by pulling them apart with two controller driven linear translation stages moving towards opposite directions, while being heated by a propane/butane mix torch. The pulling length and optical transmission through fiber were continuously monitored and recorded by a custom built software. Silica tapered fibers with sub-micron waist diameters were obtained within seconds after the oscillatory optical transmission signal transforms into a stable signal, indicating the tapered diameter was reduced to enable only a single optical mode to be guided.

Fluid dynamic simulation: A two dimensional axisymmetric numerical finite element method simulation was performed using the software COMSOL for the modeling of heat-mediated microstructure formation. A level-set function $\phi(x,y,t)$ was coupled with Navier-Stokes (NS) equations for a Newtonian fluid $\rho \left(\frac{du}{dt} + u \cdot \nabla u \right) - \nabla \cdot \left[\eta \left(\nabla u + \nabla u^T \right) \right] + \nabla p = \gamma \kappa n \delta$, where u is the velocity of an arbitrary point of the fluid, η is the viscosity, p is the pressure, ρ is the density and γ is the interfacial energy.[S1, S2] The level-set function ϕ was defined as a signed distance function, where the interface between the two fluids was determined by the level-set function at $\phi = 0.5$. The normal and curvature were determined from the level set function as $\hat{n} = \frac{\nabla \phi}{|\nabla \phi|}$ and $\hat{k} = -\nabla \cdot \frac{\nabla \phi}{|\nabla \phi|}$, respectively. The coupled Navier-Stokes equation and the level-set function were simultaneously solved by using the Fluid Dynamics Module in COMSOL. To decouple the thermal diffusion from the NS equations during the simulation, we performed 3D thermal diffusion simulation of our structure from room temperature to 300 ºC and found that a homogeneous temperature distribution was reached in less than one second (0.3 s), which is negligibly smaller than the characteristic time of the fluid flow (hundreds of seconds).

**Fabrication of As$_2$Se$_3$ Core PES Cladding Fibers**
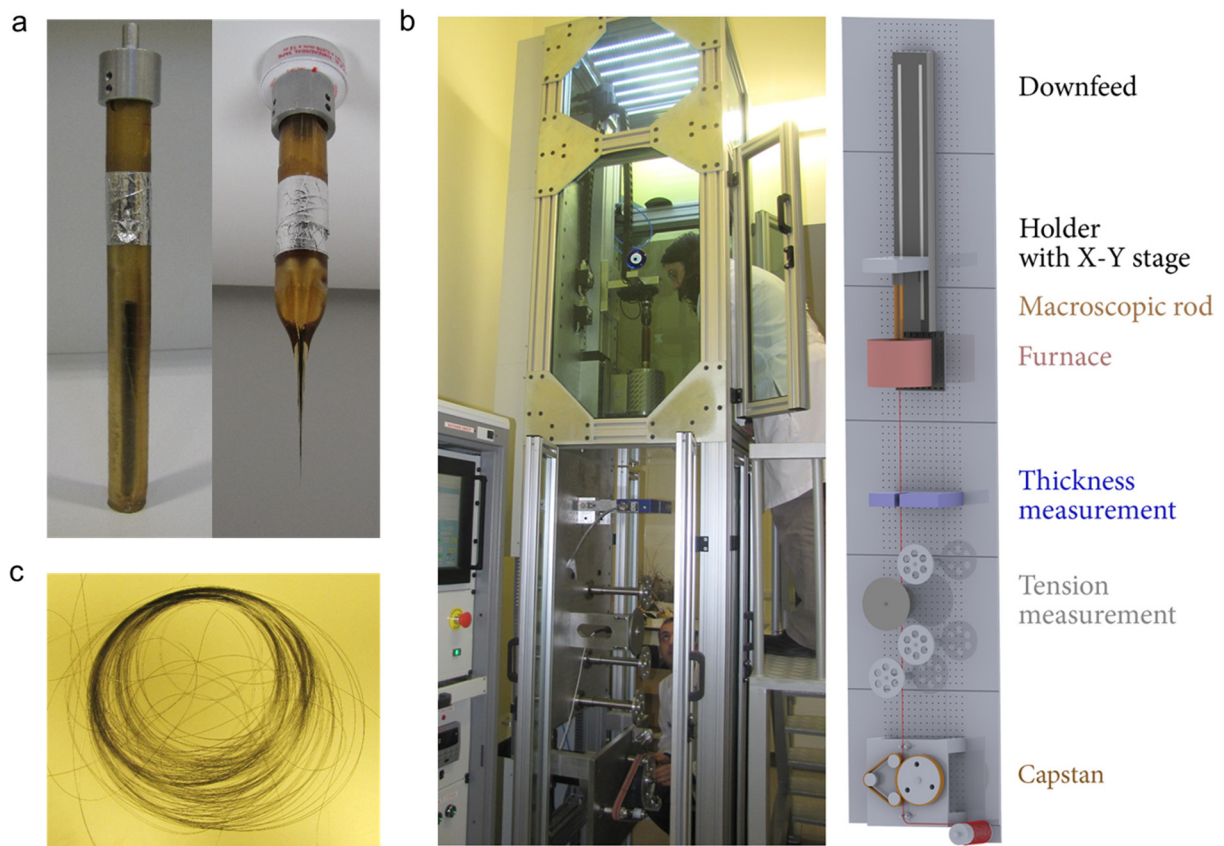
Figure S1. Fiber drawing process has two stages: fabrication of the initial preform structure and production of fibers by thermal drawing of the preform under high stress and temperature. (a) A preform structure with 6 mm core and 30 mm outer diameter, which is a macroscopic copy of the fiber, was prepared by rolling 100 μm thick PES polymer films around an As$_2$Se$_3$ rod. Before consolidation process, the preform was held under 2×10^{-2} Torr vacuum at 180 ºC for 4 hours in order to evacuate trapped air between polymer layers. Then, rolled films were consolidated in a vacuum oven at 252 ºC for 30 minutes under 2×10^{-2} Torr vacuum. (b) Fiber drawing process was executed in a custom made fiber tower which consists of a preform feeding mechanism, preform position alignment stage, furnace, optical thickness measurement system, tension measurement and a capstan. Approximately 3 MPa force was applied to the preform during heating of the preform up to 300 ºC above glass transition temperature of As$_2$Se$_3$ and PES. (c) Picture of the produced As$_2$Se$_3$ core PES cladding fibers. Volume reduction of the preform, which determines the final diameter of fiber, was controlled by the applied force and the furnace temperature.

Formation of spherical microresonators in centimeter long polymer fibers
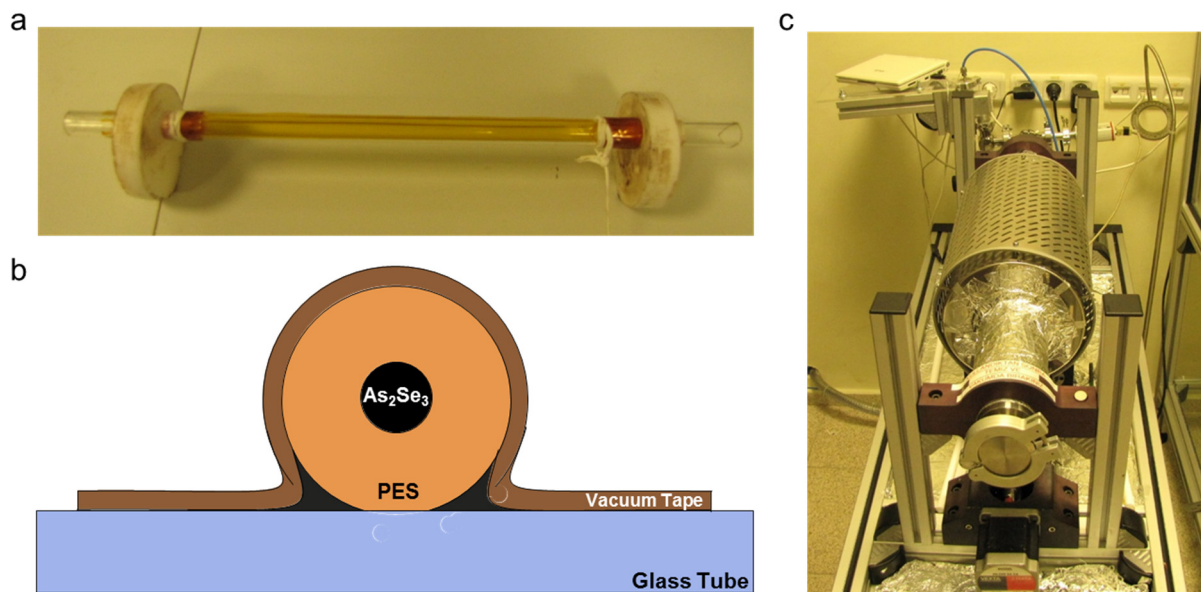

Figure S2. In order to produce a long chain of uniform As_2Se_3 microspheres embedded in a PES fiber, a novel method was developed, which takes the advantage of convective (non-contact) heating of fiber under a conformal cover assisting integrity and straightness of the fiber during the process. (a) A 12 centimeter long fiber was accommodated on a 10 mm diameter glass tube and (b) covered by a supporting vacuum tape (Kapton tape) which can stand high temperatures (over 320 ºC). In order to eliminate contact heating of fiber, the glass tube was isolated by two circular Teflon spacers from the walls of a custom-made tubular oven. (c) The tubular oven supplies necessary uniform heating with circular temperature distribution inducing PR instability in the fiber core. Releasing built-in stress, length of the fiber was finally reduced approximately to the half of initial length. After 15 minutes at 300 ºC, chalcogenide core polymer cladding fiber turned into a long self-assembled chain of microspheres held immobile in the cladding. After removing the cover tape and cutting uneven ends of the fiber, 5 centimeters long product, which is the longest fiber with embedded microspheres reported, was obtained at the end.

Temperature dependent viscosities of PES and As₂Se₃
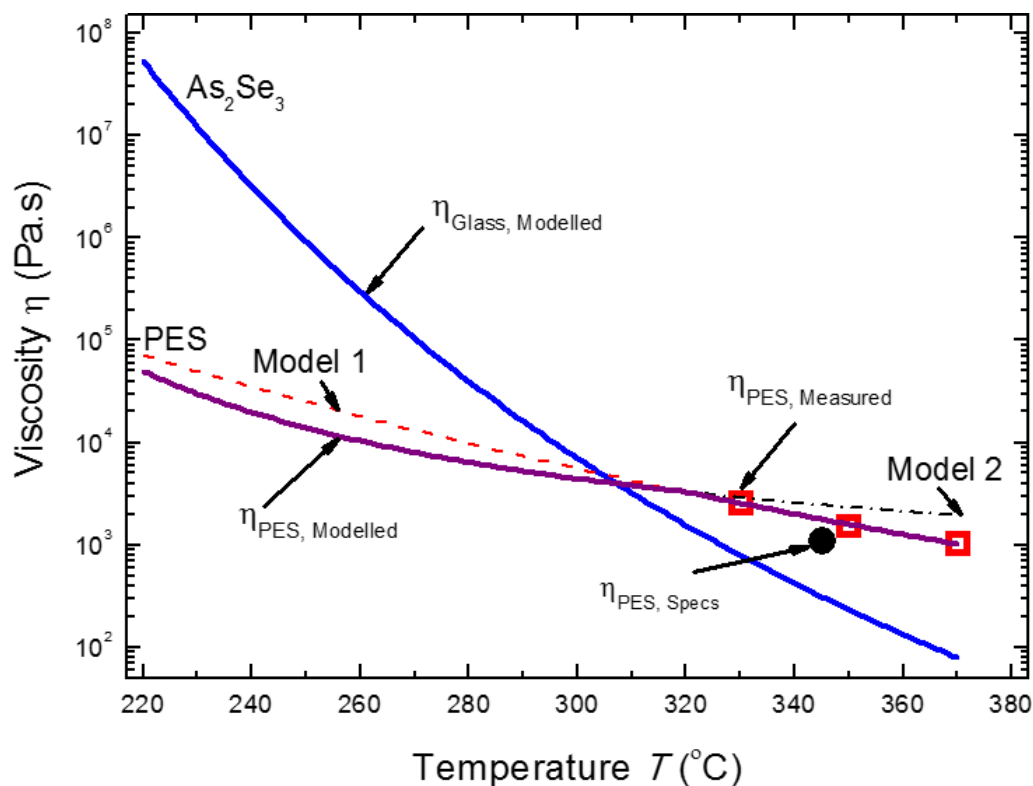

Figure S3. In our simulation, we used temperature dependent viscosities for both of the polymer cladding and the glass core. The As₂Se₃ and PES viscosities were determined by the universal logarithmic models.[S3, S4] For the PES, we could not find enough model parameters in the literature to estimate the viscosity, while other groups assumed constant viscosity for PES; therefore, we performed rheometry measurements to make sure that the viscosity used in the model was realistic and also consistent with the viscosity specified by the polymer manufacturer ($\eta_{PES, Specs}$). The PES model consists of two parts which are Model 1 (Arrhenius) for high temperatures and Model 2 with slightly varying activation energy for low temperatures.[S4] Even the first order approximation of all Arrhenius relation gives more accurate modeling of PES viscosity than assuming a constant viscosity. This is because the viscosity contrast determines not only the instability wavelength, but also the characteristic time.

Fractal process of microsphere formation by Plateau-Rayleigh instability
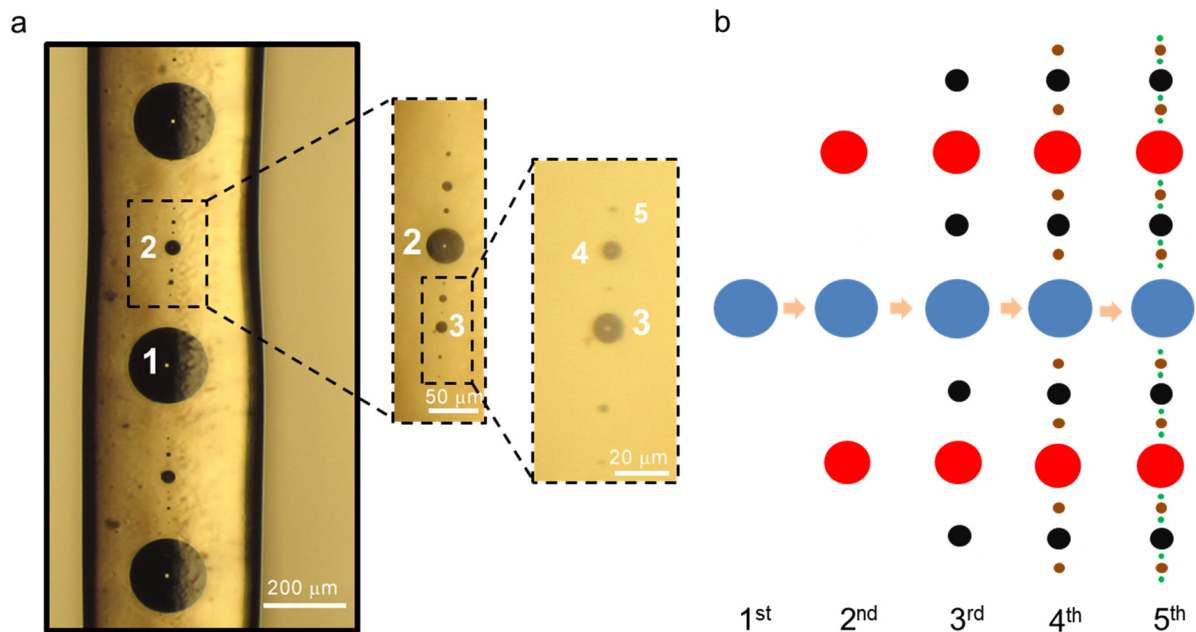
Figure S4. (a) Optical microscope pictures show fractal nature of PR instability occurring in a fiber core. Successive optical micrographs of the fiber, showing inner structure with increasing detail were taken by using 5X, 10X and 20X objectives, respectively. Although the process is self-quenching after a number of generations finally reaching submicron scales, satellite and sub-satellite sphere formation between main spheres (the first generation) can be seen down to 5th generation. Numerical simulations also reveal same fractal pattern of in-fiber sphere formation. Numbers 1-5 in the figures indicate number of sphere generations. (b) Rule of thumb is as simple as graphically represented by the figure; i.e., for every next generation, two smaller satellite spheres are supposed to reside at the sides of larger spheres of previous generation.

Theoretical comparisons of instability wavelength with experimental data
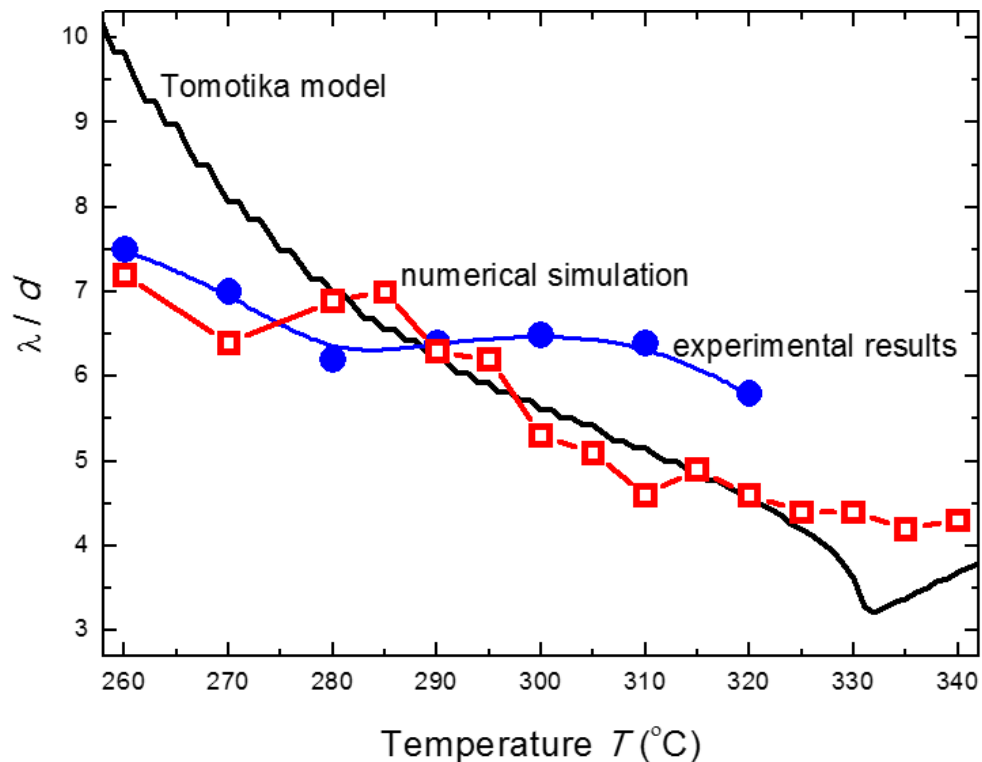
Figure S5. Comparison of the temperature dependent normalized (with respect to the initial core diameter *d*) average instability wavelength λ of experimentally produced micro-spheres and theoretically calculated data based on Tomotika model[S5] and our 2D finite element numerical simulation. At low temperatures, the simulation coincides very well with the experiment, while Tomotika model over-estimate the instability wavelength. When the temperature is increased, both the simulation and the analytical models under-estimate the experimentally measured instability wavelengths. The best agreement between the three data sets is at moderate temperatures (*T* = 280-300 °C). Therefore, we chose this range for comparing the results of experiments and simulation of sphere formation in Figure 1, Movie S1 and Movie S2.

Characteristic time of fiber core break-up
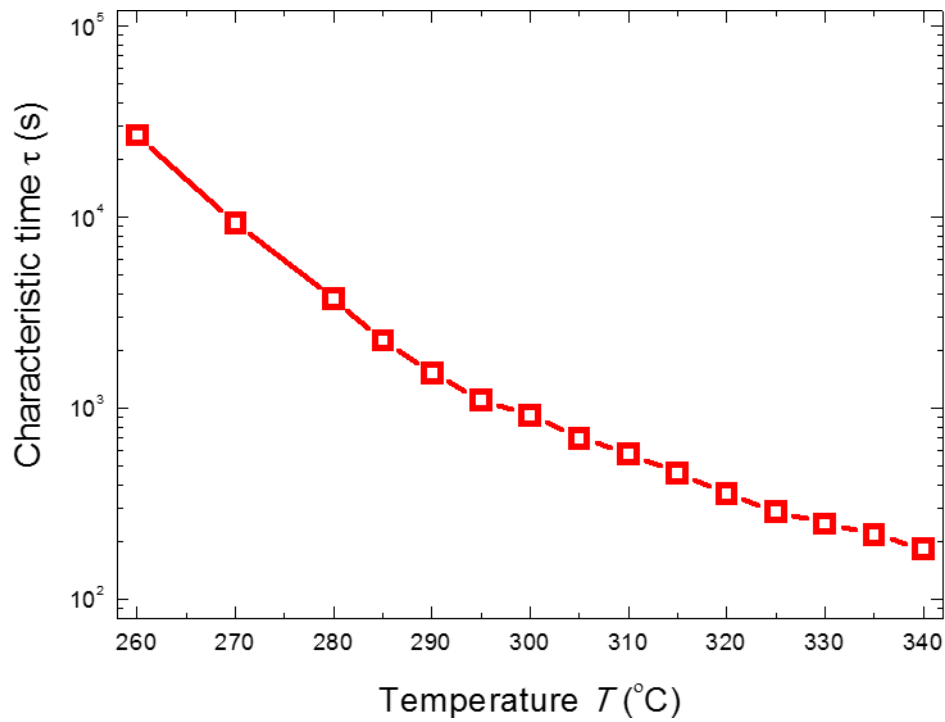
Figure S6. The variation of the characteristic time (τ) as a function of temperature T. The characteristic time is defined as the time at which the break-up starts. The logarithmic decrease of τ with temperature follows two different activation regions intersecting at a point, which coincides with the viscosity contrast turning point (around 310 °C as in Figure S3)

Microresonator array deformation setup
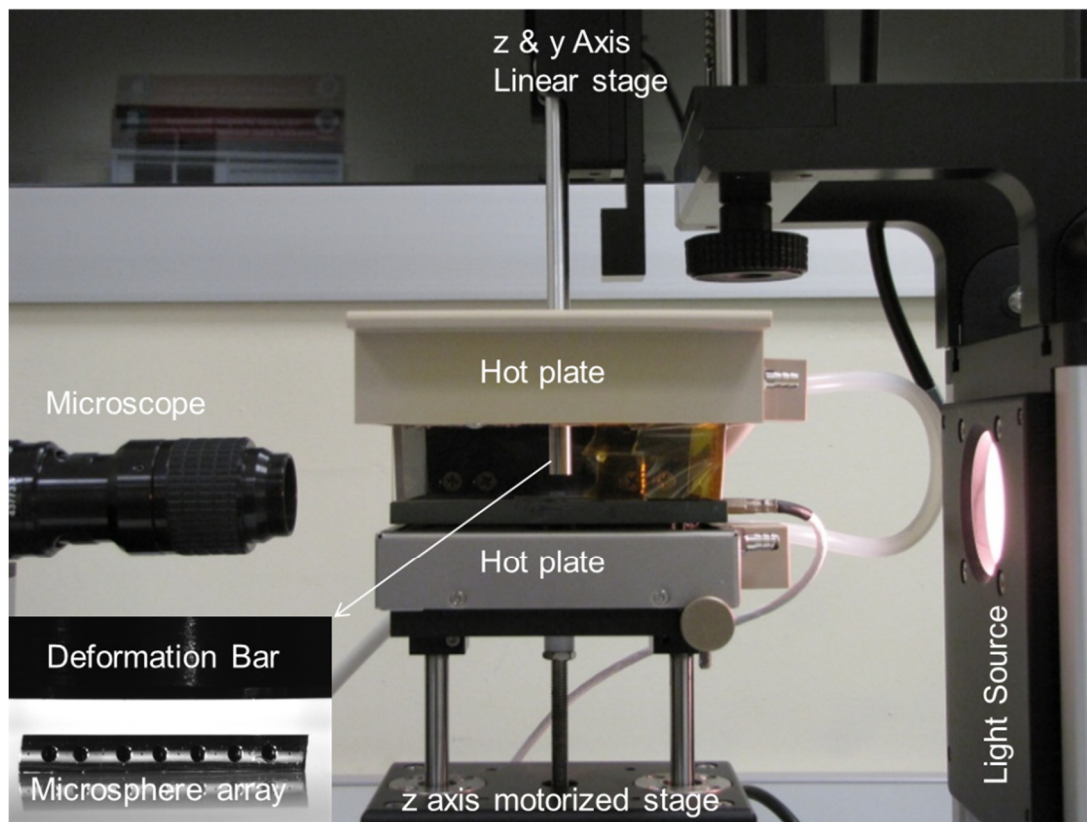
Figure S7. Experimental setup used for deformation and integration of microresonator arrays is actually a contact angle measuring system (DataPhysics OCA30) possessing a high temperature furnace (up to 400ºC) with temperature control. The system consists of a CCD camera, a long working distance microscope and a light source for process monitoring, an electrical furnace with two hotplates on top and bottom sides, and a z axis motorized stage under the furnace and a cylindrical bar attached to a z & y axis linear stage for alignment and deformation operations. Inset shows a fiber with embedded microspheres ready to be compressed.

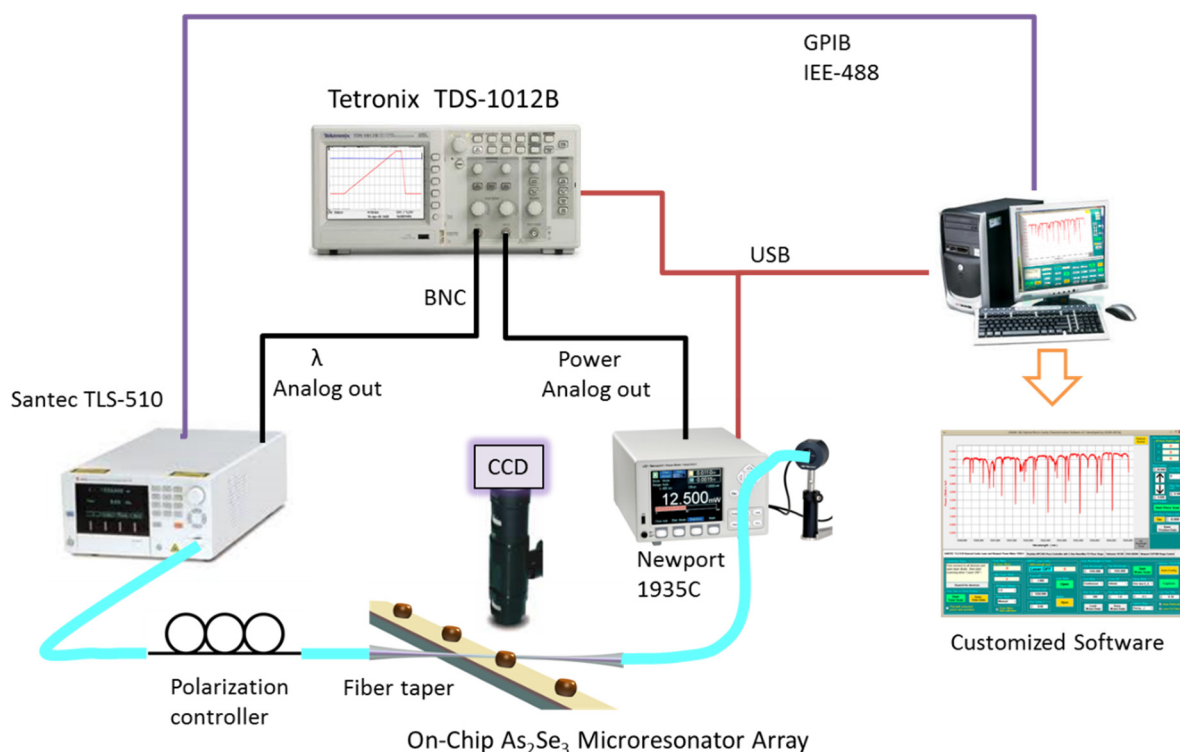**Characterization of microresonator material composition**
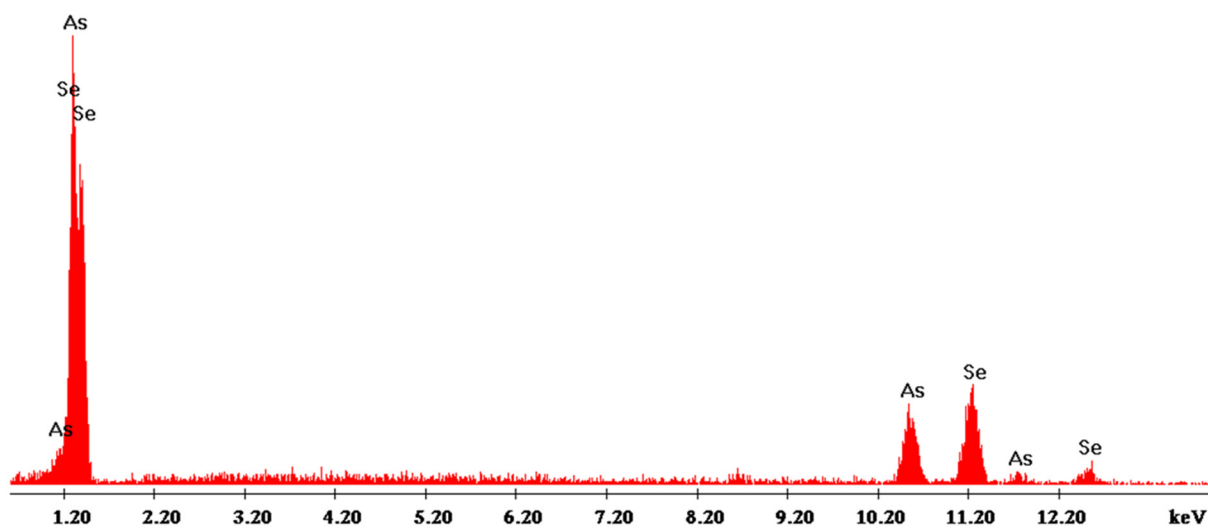
Material : As_2Se_3

| Elem	Wt %	At %	K-Ratio	Z	A	F
AsK	38.24	39.49	0.3858	1.0152	0.9937	1.0000
SeK	61.76	60.51	0.6137	0.9905	1.0033	1.0000
Total	100.00	100.00				

Figure S8. Energy dispersive X-ray spectroscopy (EDX) results obtained from on-chip microsphere resonators which were extracted out of their PES polymer encapsulation using DCM. EDX is attached to FEI Quanta 200 FEG SEM system. Peaks represent consistence of the atomic ratio of As_2Se_3. Besides, there was no impurity or residual polymer observed on the surface of microspheres after the dissolution process.

Experimental setup for optical characterization of the microresonators

Figure S9. Experimental setup used for the optical characterizations of the on-chip microresonator arrays consists of an external cavity tunable laser (Santec TLS-510, 500 kHz linewidth, 1500-1630 nm range), a polarization controller, an optical power meter (Newport 1935C with 918D-IR-0D3R detector), an oscilloscope (Tektronix 1012B) , a color CCD camera (Hitachi) with long working distance objective system (Optem Zoom 70XL), and 3-axis closed loop piezo translation stage with controller (BPC303 Controller, NanoMax-TS piezo stage with 5 nm position resolution) which is not shown in the figure. In order to begin optical characterizations, one of the resonators in the microresonator array was positioned by the piezo stage close to a tapered fiber assuring alignment with the equator of resonator, and polarization was adjusted for optimum light coupling. Laser wavelength can be scanned continuously for a desired wavelength range up to 100 nm with scan rates from 1 nm.s^{-1} to 100nm.s^{-1}. For single mode measurements, we set scan range as 50 pm and scan rate as 1 nm.s^{-1} in order to increase wavelength resolution (sub-picometer). Data acquisition from the oscilloscope was handled by a custom developed software. First channel (X axis) of the oscilloscope was connected to analog output port of external cavity laser producing a chain of triangular voltage pulses corresponding to the wavelength scan range and second channel (Y axis) was connected to output port of optical power meter to measure the transmission. Using acquisition of dual channel data in X-Y format provides optical transmission spectrum of microcavity under test. The custom software handles data acquisition and calibration process as well as adjusting configuration settings and management of communications with devices using data buses shown in the Figure.

Thermo-optic effect in chalcogenide microresonators
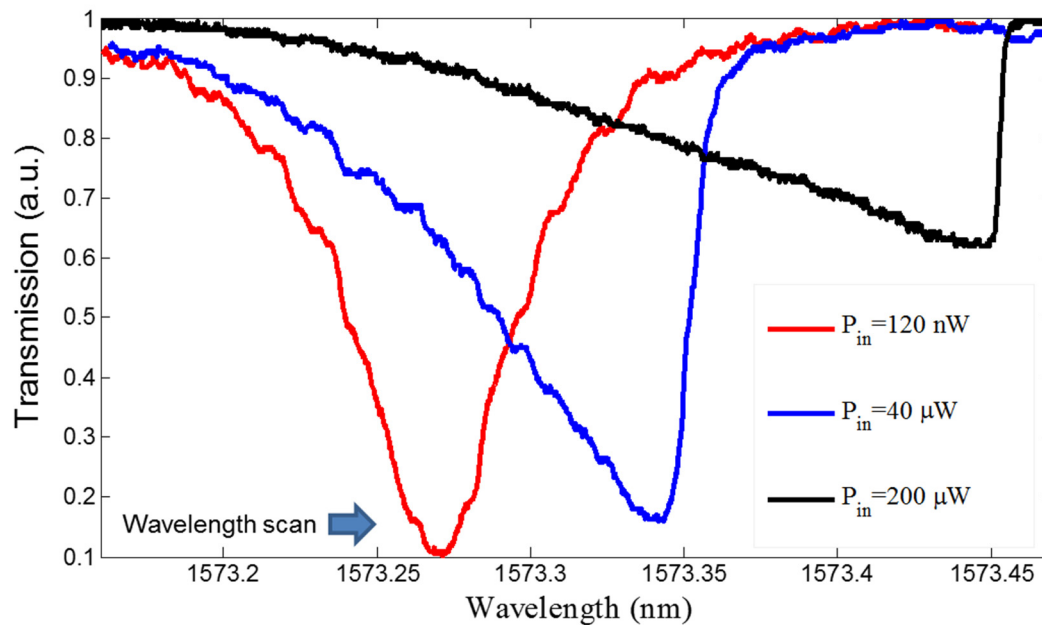
Figure S10. The resonance dips in the spectra of As_2Se_3 microresonators were observed to red-shift with increasing incident powers for both directions of wavelength scans. Although an unshifted resonance dip (red), which was captured using very low optical powers with 300 pm scan range and 1 nm.s^{-1} scan speed, has a regular Lorentzian shape, red-shifted versions of the resonance mode (blue, black) have characteristic "shark fin" shapes.[20] Since As_2Se_3 has relatively high absorption coefficients (see Figure S12) as compared to silica in this scan range, red-shifts of modes are expected, due to the heating of the resonator via absorption of the coupled light resulting in a thermal change of the refractive index and thermal expansion of resonator diameter. Reduction in the coupling strength is another manifestation of thermo-optic effect, caused by insufficient scan speed at some power levels for which wavelength shift can be more than linewidth of the resonance mode at some point during wavelength scanning.[S6]

Optical coupling into As₂Se₃ microsphere modes with a silica tapered fiber

Optical coupling depends on the phase-matching between the tapered fiber waveguide and the sphere microresonator. This implies the similarity between the propagation constants or effective refractive indices n_{eff} which is related to the propagation constant β by;

$$\beta = \frac{\omega}{c} n_{eff} \tag{1}$$

where ω is angular frequency of light and c is the speed of light in the vacuum. Therefore, the propagation constant difference can be calculated as

$$\Delta\beta = \frac{\omega}{c}\left(n_{eff,f} - n_{eff,s}\right) \tag{2}$$

where $n_{eff,f}$ and $n_{eff,s}$ are effective indices for the fiber and the sphere microresonator, respectively. Strength of Optical coupling between a fiber and a sphere microresonator is maximum when $\Delta\beta = 0$. Another key factor for optical coupling is the field overlapping of the waveguide and resonator modes.

Propagation constant of a silica fiber for fundamental mode HE₁₁ can be calculated using $\beta^2 = k^2 n_f^2 - 2.405^2/r_f^2$, where k is the wave vector in air, n_f and r_f are the refractive index of the bulk silica ($n_f = 1.44$) and the radius of the taper waist, respectively.[S7] After propagation constants were calculated for different tapered fiber radii, they were converted into effective refractive index $n_{eff,f}$ using Equation 1. Effective refractive index $n_{eff,s}$ of the microsphere resonator can be calculated for each WGM mode (q, l, m) by using $n_{eff,s} \cong \frac{l}{x_l^q}$, where q is radial mode number, l is angular mode number, and x_l^q is size parameter of the sphere microresonator. Size parameter $x_l^q = k_l r_s$ can be determined by:[S8]

$$n_s x_l^q = \upsilon + A_q\left(\frac{\upsilon}{2}\right)^{1/3} - \frac{n\rho}{\sqrt{n^2-1}} + \frac{3A_q^2}{2^{2/3}10\upsilon^{1/3}} - \frac{n^3\rho(2\rho^2/3-1)A_q}{2^{1/3}(n^2-1)^{3/2}\upsilon^{2/3}} \tag{3}$$

where $\upsilon = l + {}^1/_2$, A_q is the qth order root of Airy function, n is the ratio of refractive index of the resonator material n_s and environment n_o (air in our case), and ρ is a polarization dependent constant which is equal to 1 for *TE* modes and $1/N^2$ for *TM* modes.

In order to calculate effective refractive indices of tapered silica fiber and chalcogenide microresonators, a MATLAB code was developed. For sphere microresonator, angular mode numbers l corresponding to resonance wavelengths in experimental scan range, were first computed for different radial mode orders q and resonator radii r_s by using Equation 3. Following the determination of l values, $n_{eff,s}$ were calculated as a function of radial mode orders q and resonator radius r_s.
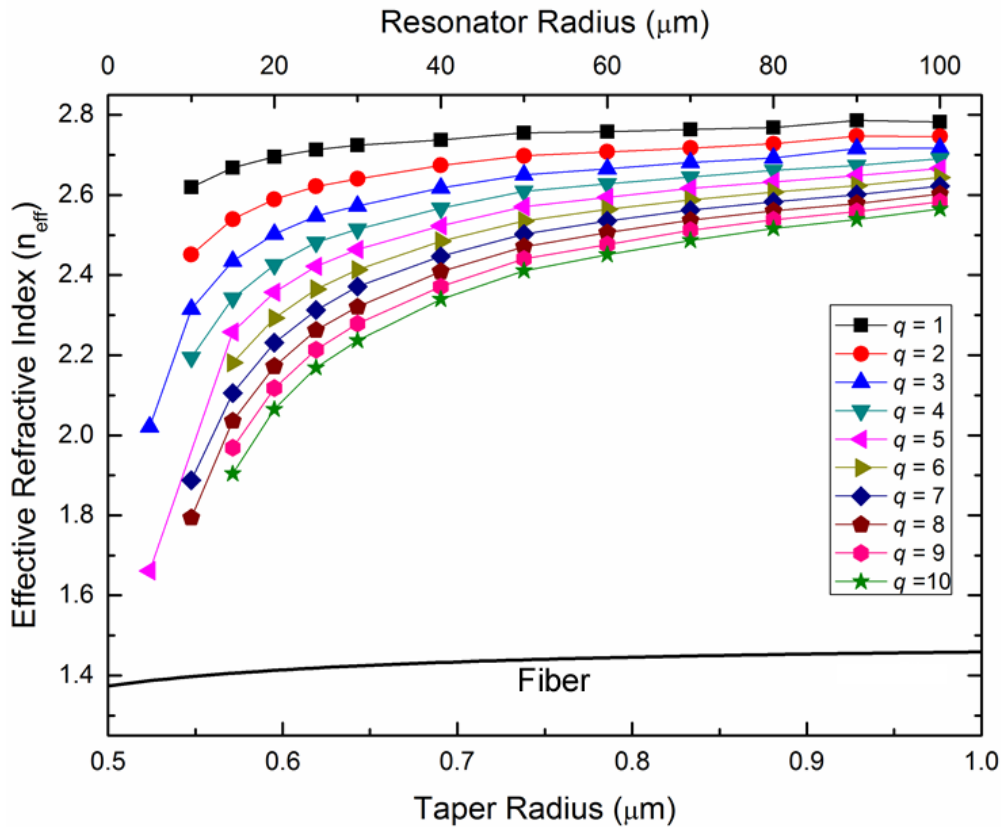
Figure S11. The effective refractive indices $n_{eff,s}$ of chalcogenide microspheres with various sizes for radial modes of different orders (q = 1, 2, 3 … 10), and effective refractive indices $n_{eff,f}$ of tapered silica fiber versus its waist radius r_f (for fundamental HE_{11} mode). Radii of the microresonator used in optical charterizations are about $R \sim 25$ μm.

Phase matching is important for optimal light coupling. Smaller the difference between the propagation constants or effective refractive indices, higher the phase matching; therefore, better optical coupling can be obtained. As seen in the Figure S11, the effective refractive index of resonator for fundamental modes (q = 1) approaches to the effective refractive index of the silica fiber with an increasing trend for smaller radii (or size parameters). Also for higher radial mode orders ($q>1$), the difference between the effective refractive indices of resonator and fiber exponentially decreases for very small resonator radii $r_s < 25$ μm. This explains why higher mode orders couples into the resonators much more favorably then the lower mode orders. In addition, achieving a smaller taper radius than the exact phase-matching taper radius can enhance the optical coupling. Because, decreased radius increases the evanescent field of the fiber which overcomes the negative effect of phase-mismatch and enhances the coupling up to a certain limit where phase-mismatch recovers its dominance over the optical coupling.[32]

Optical properties of chalcogenide As$_2$Se$_3$
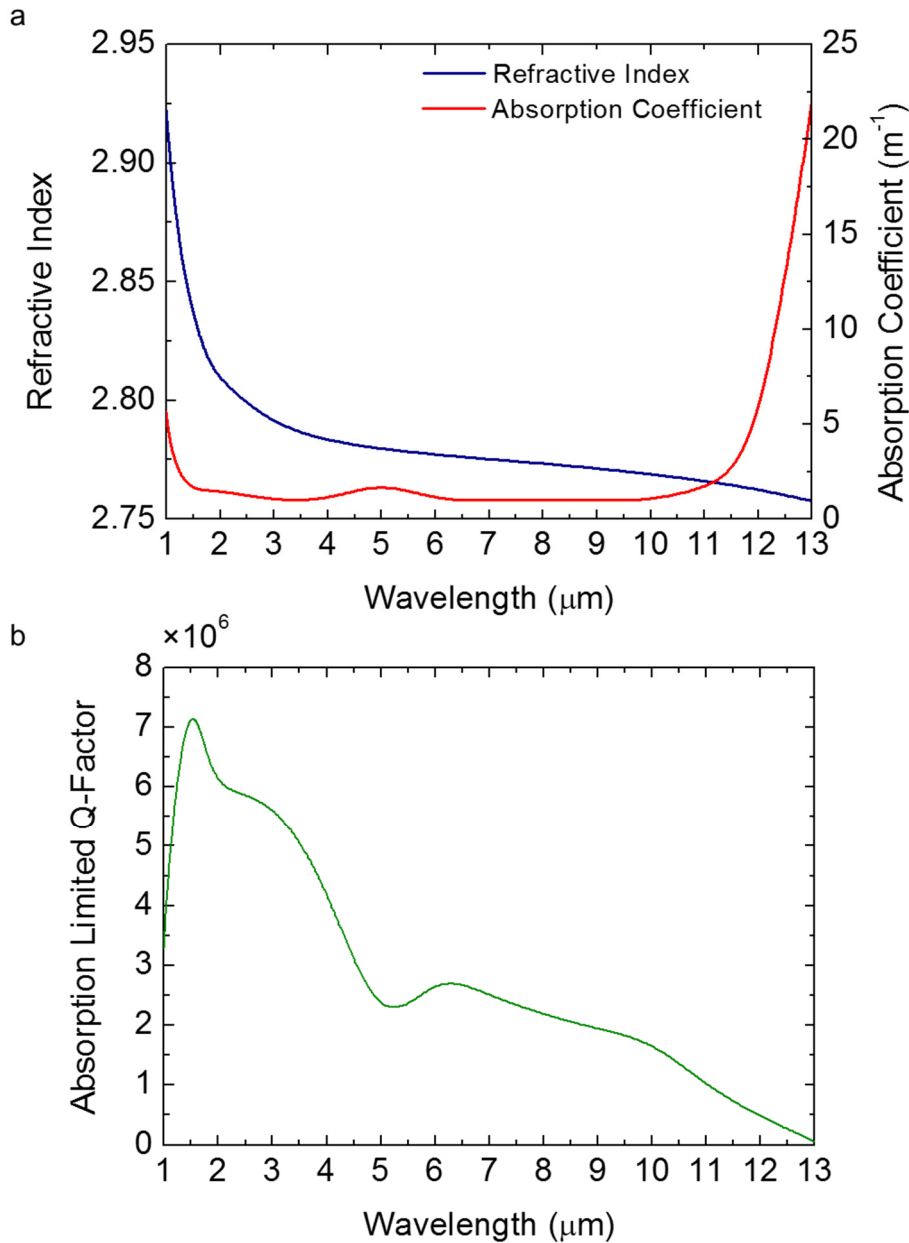
Figure S12. Optical properties of a commercial As$_2$Se$_3$ glass[S9] are given in terms of a) refractive index n and absorption α as function wavelength λ. Absorption is $\alpha = 1.6$ m^{-1} at 1550 nm. b) Absorption limited quality factor Q_{abs} can be calculated from (n, α) data, as $Q_{\text{abs}} = 2\pi n/\lambda\alpha$.[33] Q_{abs} for As$_2Se_3$ is found to be 7.2×10^6 for $\lambda =$ 1550 nm and $n = 2.83$, which is an upper bound for intrinsic Q-factors in the case of ultra-smooth and clean resonator surface. Although As$_2$Se$_3$ has relatively high absorption compared to silica restricting its use as nonlinear optical material, it is a very promising material for microresonators in mid-IR applications, due to low absorption and high Kerr nonlinearity.

Movie of simulation of in-fiber micro-sphere formation by PR instability

SI_S.wmv (1.87 MB)
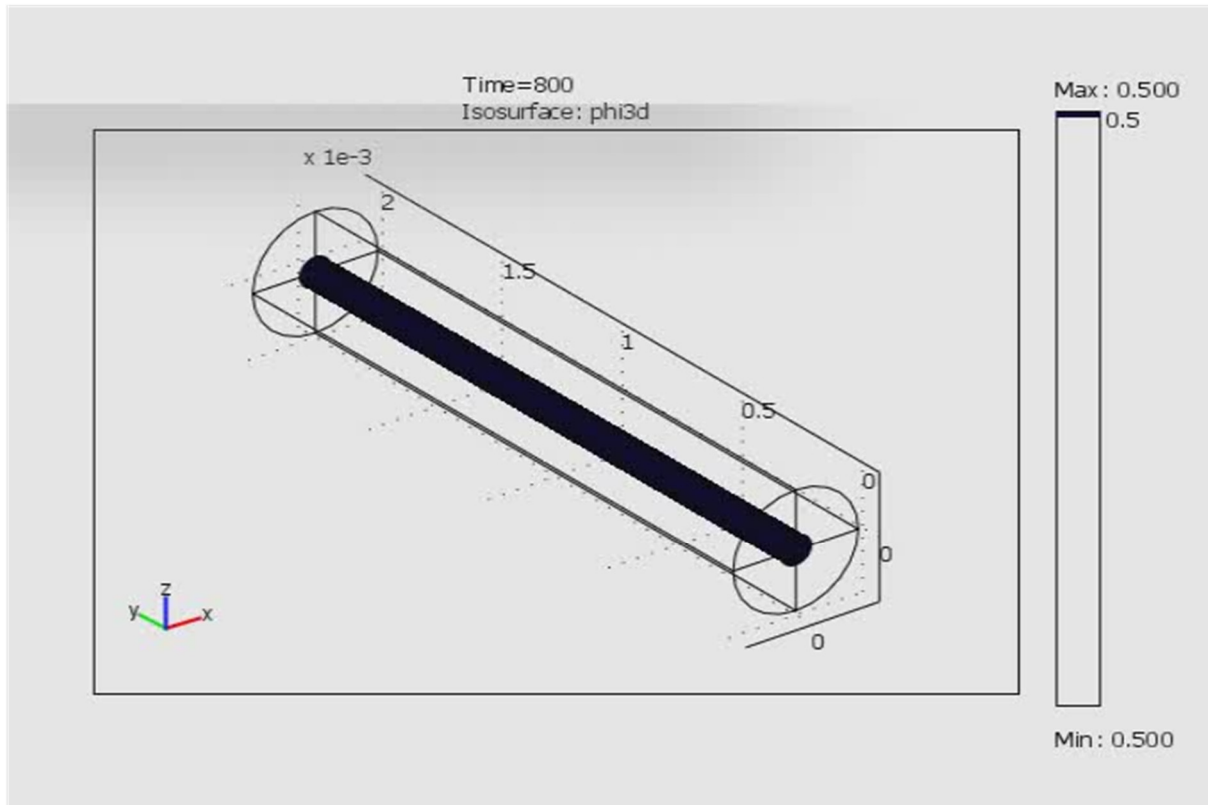
Movie S1. COMSOL simulation of the PR fluid instability in an As_2Se_3/PES core/shell fiber at 300 °C. The isosurface shows the outer surface of the chalcogenide core during the sphere formation. The satellite spheres in addition to main spheres can be seen in the video. The dimensions in the simulation are chosen to emulate the reality. The core has a diameter of 80 µm inside a PES cladding with outer diameter of 400 µm.

Movie of in-fiber micro-sphere formation by PR instability

SI_E.wmv (3.85 MB)
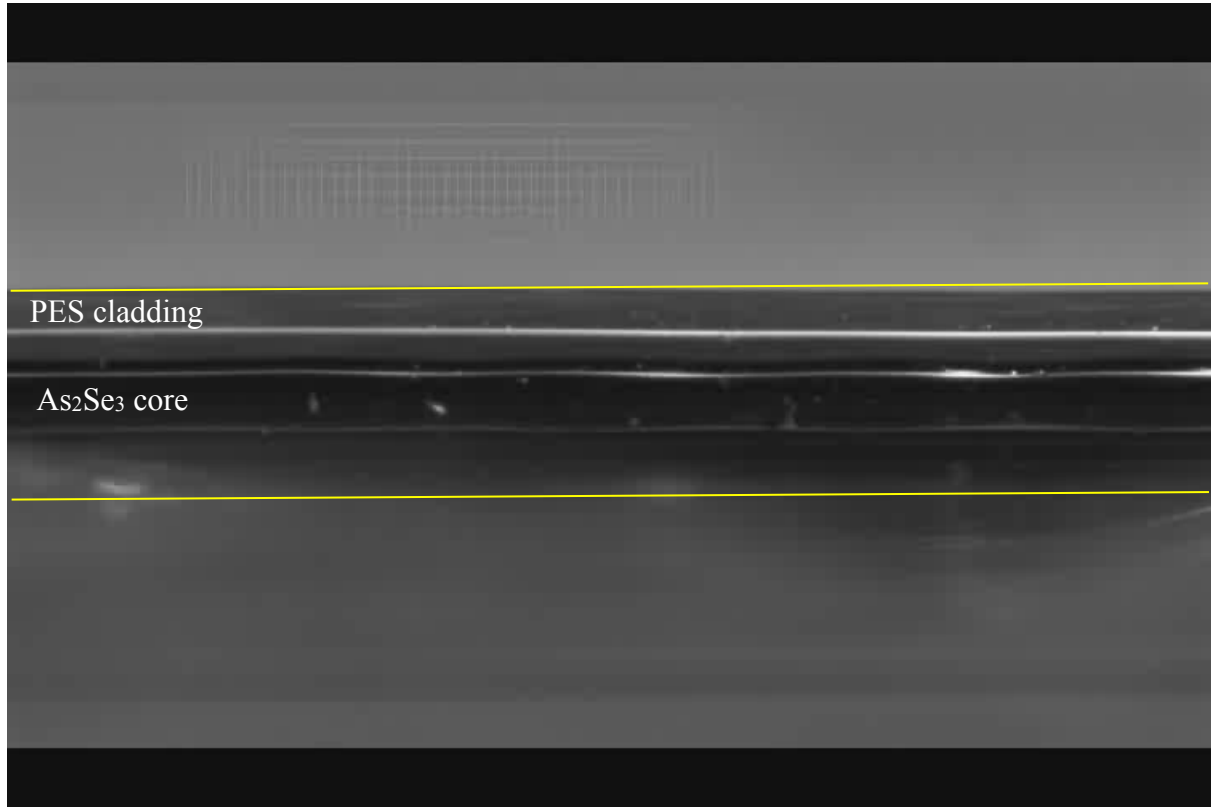

Movie S2. Real footage of As_2Se_3 fiber core break-up at 300 ºC, due to Plateau-Rayleigh instability resulting into a necklace of self-assembled micro-spheres embedded in the fiber. Satellite and sub satellite sphere formation can also be seen between main spheres. Prolate ellipsoidal appearance of spheres is a result of the fiber surface acting as a cylindrical lens.

Movie of optical coupling into ellipsoidal microcavity with a silica tapered fiber

ellipsoidalCavity.wmv (817 KB)
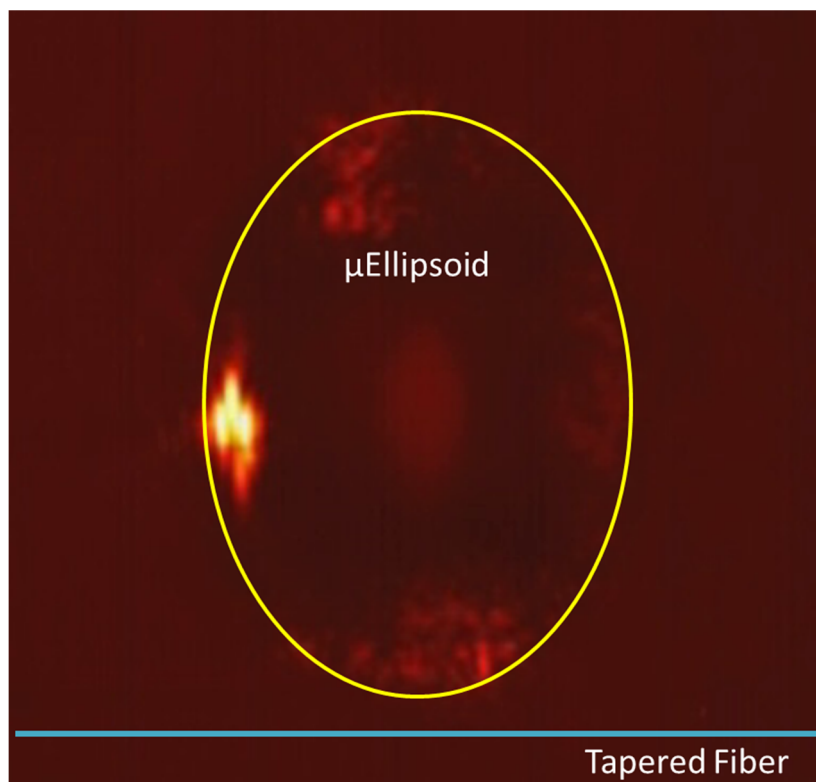
Movie S3. This movie, recorded by a thermal camera, shows optical coupling to an ellipsoidal microcavity using a silica tapered fiber approaching from the bottom. Bright spot on the left in the middle is an ambient scattered light reflected from the surface, which is irrelevant to optical coupling with the tapered fiber.

References

[S1] E. Olsson, G. Kreiss, *J. Comput. Phys.* **2005**, *210*, 225.

[S2] B. Chinè, M. Monno, *Proc. COMSOL Conference* **2010**.

[S3] A. S. Tverjanovich, *Glass Phys. Chem.* **2003**, *29*, 532.

[S4] C.-Y. Liu, J. He, R. Keunings, C. Bailly, *Macromolecules* **2006**, *39*, 8867.

[S5] S. Tomotika, *Proc. R. Soc. Lond. A* **1935**, *150*, 322.

[S6] M. Borselli, T. J. Johnson, O. Painter, *Opt. Exp.* **2005**, *13*, 1515.

[S7] J. C. Knight, G. Cheung, F. Jacques, T.A. Birks, *Opt. Lett.* **1997**, *22*, 1129.

[S8] S. Schiller, R.L. Bayer, *Opt. Lett.* **1991**, *16*, 1138; C.C. Lam, P.T. Leung, K. Young, *J. Opt. Soc. Am.* B **1992**, *9*, 1585; S. Schiller, *Appl. Opt.* **1993**, *32*, 2181.

[S9] B. Ung, M. Skorobogatiy, *Opt. Express* **2010**, *18*, 8647.